

## **MODELING AND CHARACTERIZATION OF MICROTUBULAR IT-SOFC SYSTEMS**

**N. Sammes, J. Song, B. Roy, K. Galloway**

Department of Metallurgical and Materials Engineering  
Colorado School of Mines  
1500 Illinois Street, CO 80041, USA  
Tel: 303 273 3344  
Fax: 303 273 3057  
Email: nsammes@mines.edu

**T. Suzuki, M. Awano**

Functional Assembly Technology Group  
Advanced Manufacturing Research Institute,  
AIST, Nagoya, Japan

**A M. F. Serincan**

Connecticut Global Fuel Cell Center,  
University of Connecticut, Storrs, CT, USA

### **Abstract**

Sub-millimeter range micro-tubular SOFCs have been modeled, designed and tested in the intermediate temperature range of 450~550 °C. The results of a two-dimensional, steady state, non-isothermal computational model incorporating radiation, heat transfer, flow and transport of species in the porous gas diffusion electrodes are presented and compared to the experimental data. The mechanical tests with electrolyte coated and uncoated Ni-GDC anode micro-tubes were tested using a burst test system, and showed the effect of a number of variables on the burst strength, including variation of pore-former and tube thickness. In the intermediate temperature range of 450~550 °C the performance of 0.8 mm diameter micro-tubular ceria-based SOFCs was found to be between 110~350 mW·cm<sup>-2</sup>.

### **KEYWORDS**

Microtubular SOFC, SOFC, cerium oxide, mechanical burst strength, modeling, electrochemistry

### **INTRODUCTION**

Solid oxide fuel cell (SOFC) has been considered as an alternative source of energy due to their high electrical conversion efficiency, superior environmental performance, and fuel flexibility [1-3]. In comparison to conventional SOFC's, micro tubular (MT) SOFC's [4, 5] have many advantages such as high resistance to thermal shock and higher power densities [6, 7]. Therefore, improving the power density at reduced operating temperatures allows for using cost-effective materials for interconnects and balance of plant [8-10]. In this work, we characterized the MT-SOFC which has the materials configurations of NiO/GDC-GDC-LSCF. Fabricated MT-SOFC was characterized using the modeling and electrochemical testing to predict a MT-SOFC performance as well as burst test to understand the mechanical properties. For the accurate modeling of the microtubular SOFC, A two-dimensional (2D), axial symmetric, steady state, non-isothermal computational model incorporating radiation heat transfer, flow and transport of species in porous gas diffusion electrodes has been applied in which anode, cathode, electrolyte and flow channels are modeled as separate domains to have an accurate characterization of the system, which also includes the surrounding heat source. For the mechanical testing of the cell, a burst testing method, using pressurized water was applied. Electrochemical

performance adopting a new current collection method and novel electrochemical characterization method was introduced.

## MODELING AND SIMULATION

The modeled geometry is based upon micro tubular cells fabricated as a part of the Advanced Ceramic Reactor Project (ACRP) initiated by New Energy and Industrial Technology Development Organization (NEDO) of Japan. The single cell tests are assumed to be carried out in a firebrick furnace in which the heat is supplied by the wires surrounding the cell so that there is an even peripheral heat distribution.

### Model Description

This study employs two separate models in order to have a more accurate representation of the fuel cell test system used in the experimental studies while not cutting down the computational efficiency: furnace model, fuel cell model.

Furnace model is bestowed to concentrate on the transport phenomena in the furnace and the surrounding room atmosphere and appraise the transport properties at the boundaries of the fuel cell model domain which is abridged from the furnace model domain. The furnace model consists of the furnace, fuel cell as a whole, fuel channel and the surrounding room atmosphere. The difference between the furnace temperature and the room temperature invokes the natural convection which transmits the air to the fuel cell. To implement natural convection in the model, non-isothermal flow equation is used instead of Bousinesq approximation applied to Navier-Stokes equation.

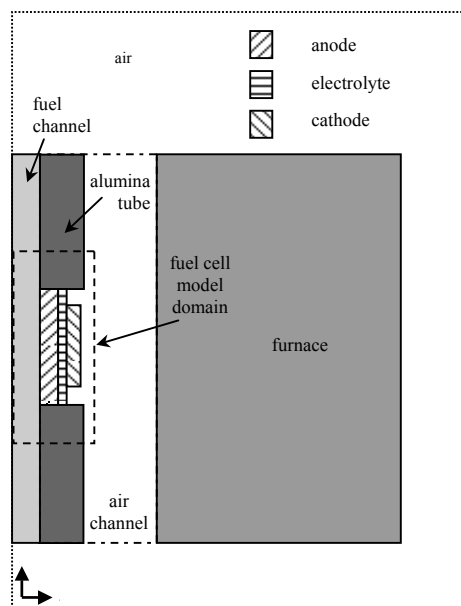


Fig. 1. Model geometry. Dashed lines show the boundaries of the fuel cell model domain

On the other hand fuel cell model incorporates heat, momentum, species and charge balances. Heat equation is solved for all modeled domains. In fuel channel and porous electrodes species balance is taken into account in the form of Maxwell-Stefan equation. Non-isothermal Flow equation is solved in the fuel channel whereas in the electrodes the momentum equation is modified in the form of Brinkmann equation to cover the transport phenomena in porous media. In the air channel, only heat equation is solved while species properties are estimated from the furnace model and given as boundary conditions at the cathode inlet. Electronic and ionic charge balances are implemented in the form of Ohm's Law throughout the anode, electrolyte and the cathode domains.

Fuel cell model also takes into account of electronic charge transport in the electrolyte which is a phenomenon resulting in OCV drops commonly seen in ceria based electrolytes under reducing atmospheres.

## Model Results

Fig. 2 a shows a uniform temperature distribution in the air channel with the exception of the rise in temperature in the cell as a result of the ohmic heating. The fuel cell model domain boundaries can be seen as the dashed lines in Fig. 2 b. Boundary condition for heat equation is given as constant temperature relying on the uniform temperature distribution in the air channel obtained from the furnace model. Fig. 2 b shows the oxygen mass fraction distribution inside the air channel at 3.8 A/cm<sup>2</sup>. Oxygen mass fraction profiles at the cathode inlet are obtained as a function of current density as are seen in Fig. 2 c. Average mass fractions are then calculated over the cathode inlet length and are specified as a function of current density at the cathode inlet as boundary conditions for species equation.

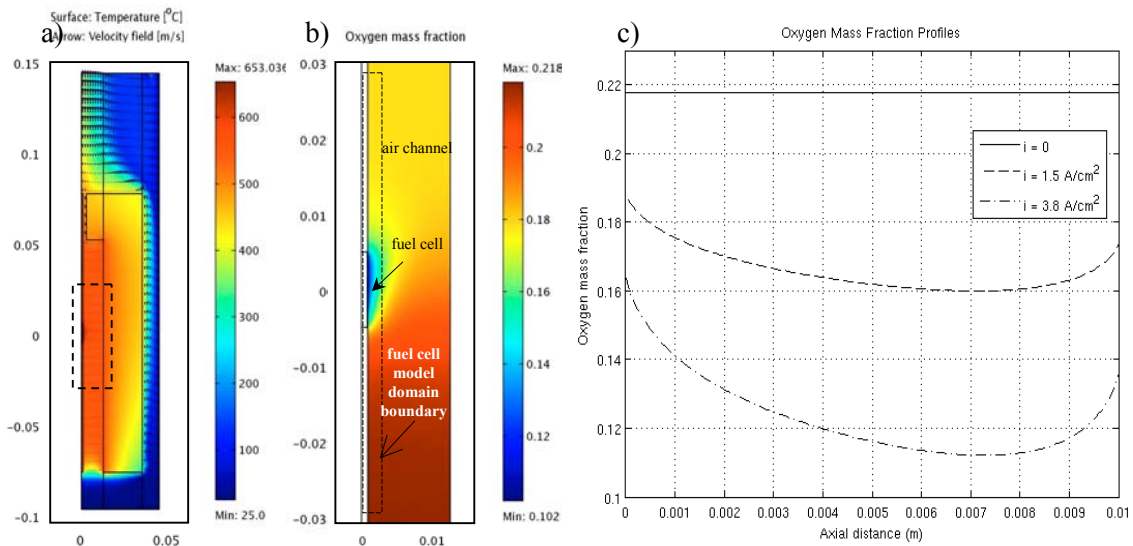


Fig. 2. a) Temperature distribution in the furnace. b) Oxygen mass fraction distribution in the region defined by the dashed lines in Fig. 2 a. c) oxygen mass fraction profiles at the cathode inlet for different current densities

In Fig. 3 model results are compared with the experimental polarization curves for 450, 500 and 550 °C. As is seen in Fig. 3 a, model results show good agreement with the experimental data. Establishing a good fit for different temperatures explain that the model captures the temperature dependency on cell electrochemistry pretty well. An important feature of the model is the inclusion of internal current leaks due to electronic conductivity of the ceria based electrolyte which results in a drop in open circuit voltage. As seen in Fig. 3 b a drop in OCV of 0.18 V is observed in the experimental results. Fig 3.b compares the polarization curve obtained when the model includes internal currents with that when internal currents are not included. The following results and discussions are held for the model results obtained for the fuel cell operation at 550 °C.

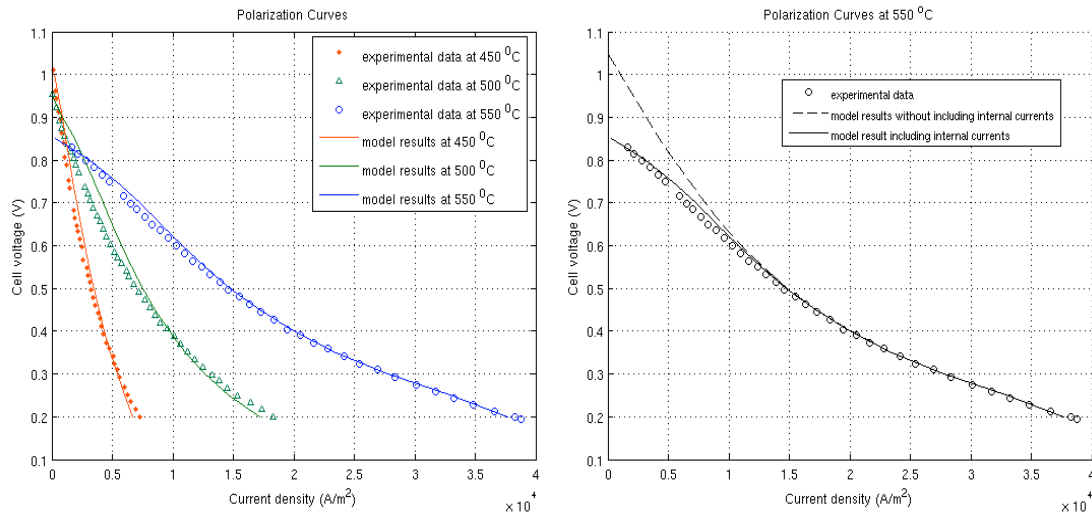


Fig. 3. a) Comparison of the polarization curves for different operating temperatures. b) Comparison of the polarization curve when internal currents are included and not included

In Fig. 4, temperature distributions in the model domain for different voltages are seen. Very similar distributions are observed both for 0.7 V and 0.2 V. At 0.7 V cell temperature increases to 562 °C, whereas at 0.2 V, owing to the extent amount of heat generation in the cell, cell temperature is found to be rising up to 668 °C. Ohmic losses, reversible and irreversible losses adds up to the heat generation which is calculated as 1.31 W at 0.2 V when output power is found to be 0.28 W.

Temperature rise in fuel channel is proportional to the rise in the cell; however, the former lags the latter due to the convective heat transfer through the channel which results in the warped temperature contours in the fuel channel as seen in Fig. 4 a-b. Fig. 4 c shows the temperature profiles as a function of cell voltage in the fuel channel. While flowing through the anode, fuel warms up and then when it encounters the alumina tube which is colder than the fuel cell it cools down again. At the same time, heat transfer from fuel cell to the fuel channel prevents further increase of the cell temperature.

Fig. 4 d shows the radial temperature profiles. Radial temperature difference is more notified in air channel than that in the fuel channel because of the fact that closed boundaries of the fuel channel restricts temperature variations. Nonetheless, about 16 °C of radial temperature difference is observed in the fuel channel at 0.2 V. There is not a significant radial temperature difference observed in the cell when it is compared with the values for gas channels.

Fig. 5 shows reactant concentration distributions and profiles along the electrolyte interfaces. Since the cathode is shorter than the electrolyte and the anode, not the entire length of anode is utilized. Anode reaction takes place in the region across the cathode coating. There is assumed to be a symmetrical cathode coating of 7 mm on the 10 mm anode - electrolyte tube. Therefore, reaction takes place from 1.5 mm above the lower edge to 1.5 mm below the upper edge of the anode.

If one discusses Fig 4.c regarding the information given above, it can be seen that the temperature difference across the catalytically active anode domain is 45 °C at cell voltage of 0.2 V when a larger temperature difference of 90 °C is observed across the whole bulk of the anode. Thus, it can be stated that having anode tube longer than the cathode coating is beneficial in terms of thermal management as any possible crack in the cell due to temperature difference will be more likely diverted to the parts of the anode which are catalytically inactive.

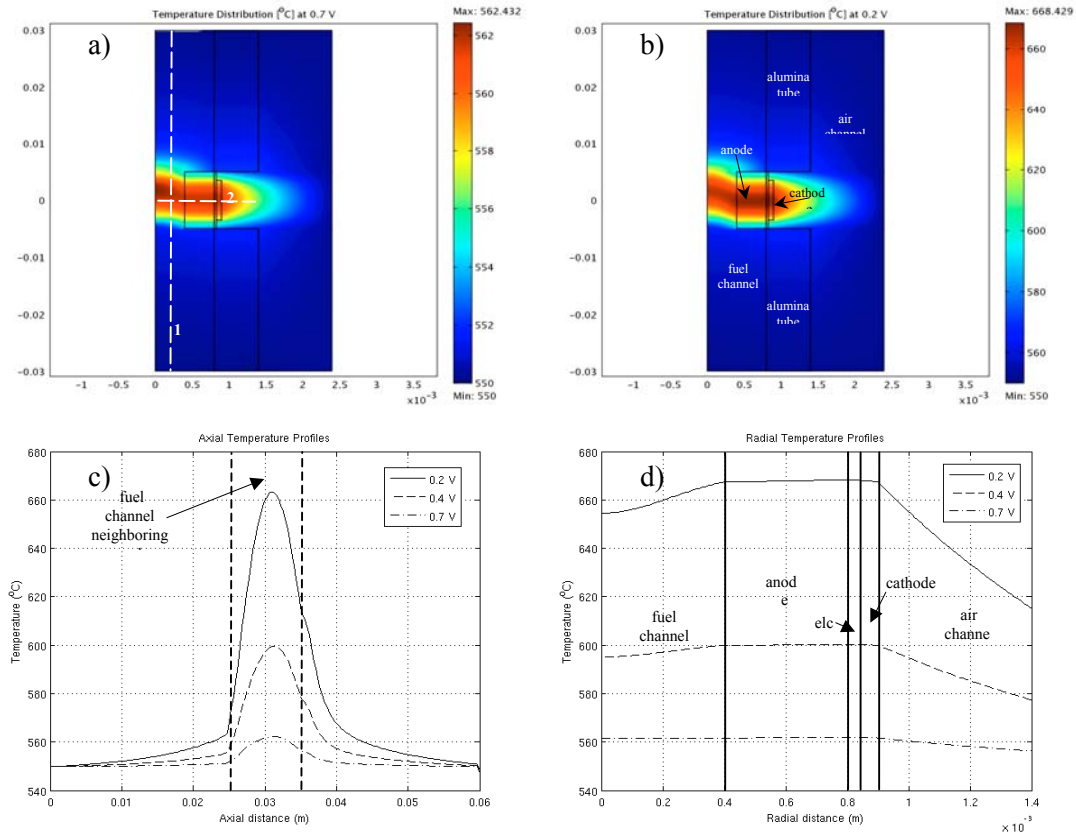


Fig. 4. Temperature distribution for a) 0.2 V and b) 0.7 V. c) Axial temperature profiles along the dashed vertical line in Fig. 4 a for different operating voltages. d) Radial temperature profiles along the dashed horizontal line in Fig. 4 a for different voltages

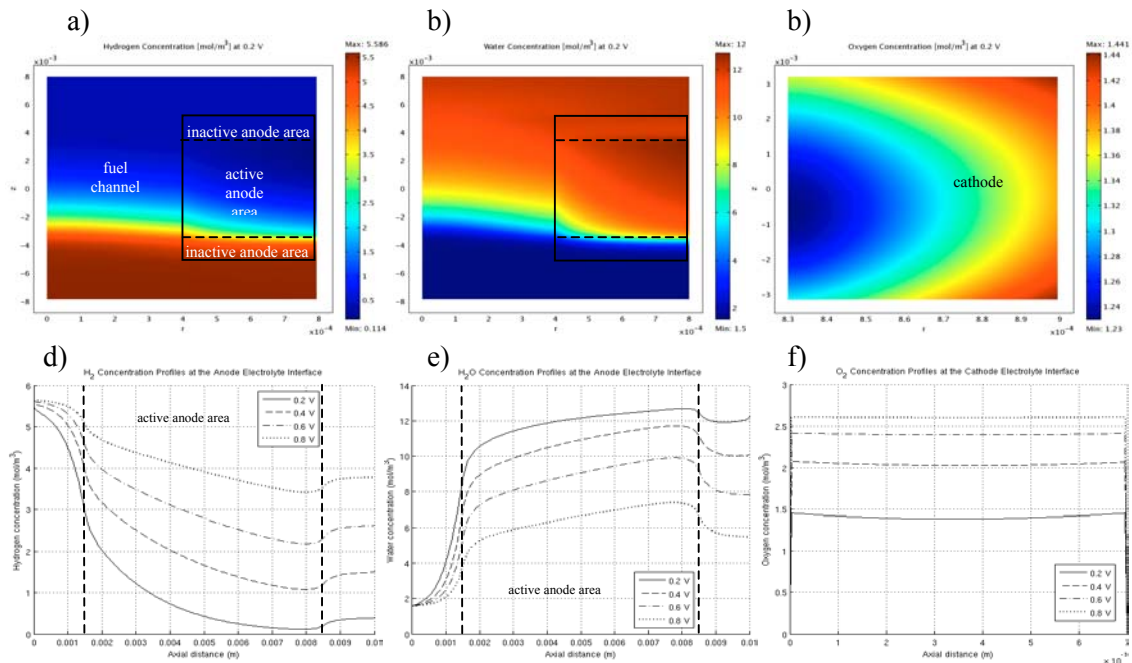


Fig. 5. Concentration distribution of a) hydrogen b) water and c) oxygen. Concentration profiles of d) hydrogen and e) water along the anode – electrolyte boundary and f) oxygen along the cathode – electrolyte boundary for different operating voltages

The effect of short cathode coating is also reflected on the concentration profiles for hydrogen and water as seen in Fig. 5 d-e. As reaction occurs in the anode hydrogen is depleted which explains the gradual drop in the hydrogen concentration profile. However, at the upper regions the chemical reaction rate decreases because it is also dependent on the reactant concentration as explicated by Butler-Volmer equation. Therefore the concentration profile has a decreasing slope at the upper regions of the anode electrolyte interface. Water concentration profiles shown in Fig. 5 e can be discussed in a similar way.

Fig. 6 shows the flow of electronic current in the anode for different operating voltages. It should be noted that at OCV conditions reaction takes place and electrons are generated but generated electrons migrate through the electrolyte and are terminated at the cathode. As a result, current can not be utilized by the external circuit. At voltages less than OCV, electrons generated at the anode split as some going through the electrolyte and the others going through the external circuit. Fig. 6 a corresponds to 0.859 V which is slightly lower than the experimental OCV. At this voltage most of the electrons generated in the vicinity of electrolyte short circuit the cell but external current density is also generated. At lower voltages external electronic current flow gets superior to internal electronic current flow. As seen in Fig. 6 d after some point, all the electrons generated during the reaction are utilized by the external circuit.

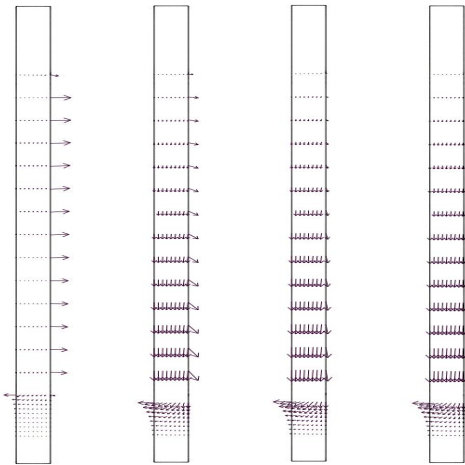


Fig. 6. Electron flow in the anode for 0.855, 0.85, 0.83 and 0.5 V

The path of the electrons completing the external circuit is determined by the current collection method. Current collection is carried out in the experiments by the wires attached to the lower edge of the anode. Consistently in the figures, arrows showing the path of the electron flow can be seen as pointing outwards from the lower edge of the anode.

Exchange current density profiles for anode and cathode are shown in Fig. 7. As expected anode exchange current density is higher than that of cathode due to the faster kinetics of the anode reaction. Even so, the area under the curves for anode and cathode are equal to satisfy the charge balance. Interpreting exchange current density as a measure of reaction rate, it can be stated that the anode reaction takes place in the 30  $\mu\text{m}$  vicinity of the electrolyte interface at 0.2 V. This outcome encourages one to decrease the thickness of the anode tube to alleviate the mass transfer losses, as long as the cell is maintained mechanically stable.

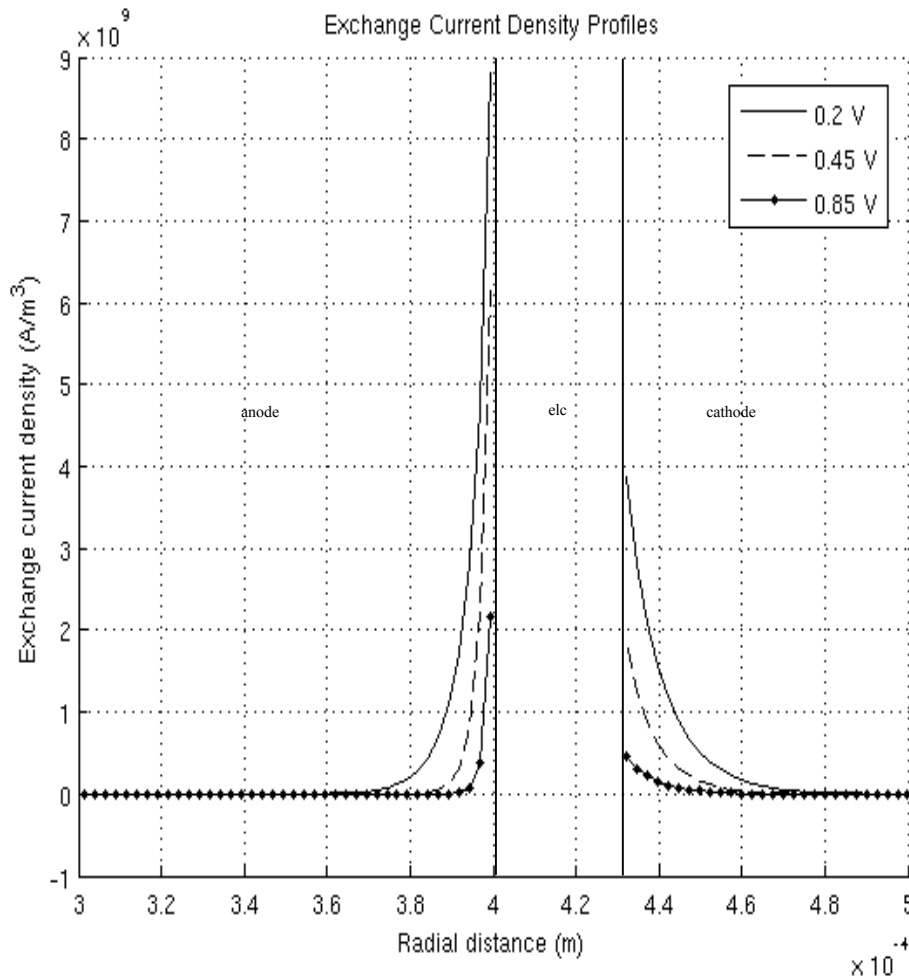


Fig. 7. Anodic and cathodic exchange current densities as a measure of the reaction rate. Although the anodic current density is bigger at the interface, integral under the curves are equal to satisfy the charge balance

### MECHANICAL TESTING

To understand the mechanical properties of micro tubular SOFC, the fabricated MT-SOFC was tested using a burst-test apparatus. The burst strength was measured under an applied water-pressure. Fig. 8 shows a picture of the burst test apparatus (right) developed for this system. The burst-test apparatus was composed of three parts; water pump to induce the water pressure into the system, pressure transducer and indicator to measure the applied pressure, and web camera to record the burst tendency after applying the pressure; as shown in Fig. 8.

Fig. 9 shows the tube specimens before testing (left side) and after testing (right side). Tube specimens were fixed onto the load cell using epoxy resin, as shown in Fig. 9. Pressurized water, up to 15,000 psi, was fed into the tube at a controlled rate to burst the tube. The pressure was recorded using the pressure indicator. The burst behavior was then recorded via the computer system. By measuring the burst pressure, the maximum pressure to withstand the gas pressure in the real system (as a hoop stress) was evaluated. The hoop stress (to failure) was determined using equation 1.

$$\sigma = \frac{PD}{2t} \quad (1)$$

where,  $\sigma$  is the hoop stress,  $P$  burst (water) pressure,  $D$  tube inside diameter, and  $t$  is the tube wall thickness.

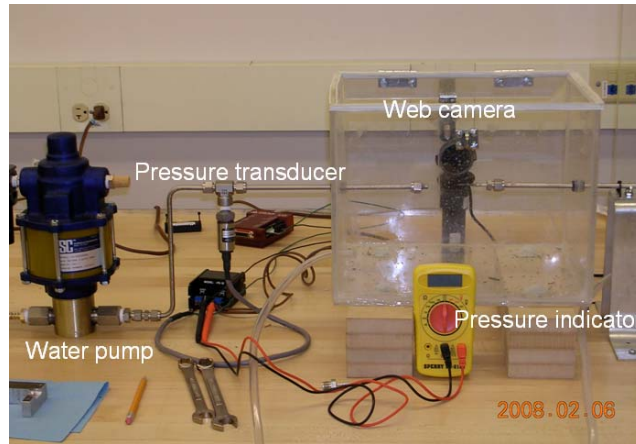


Fig. 8. Burst strength testing apparatus

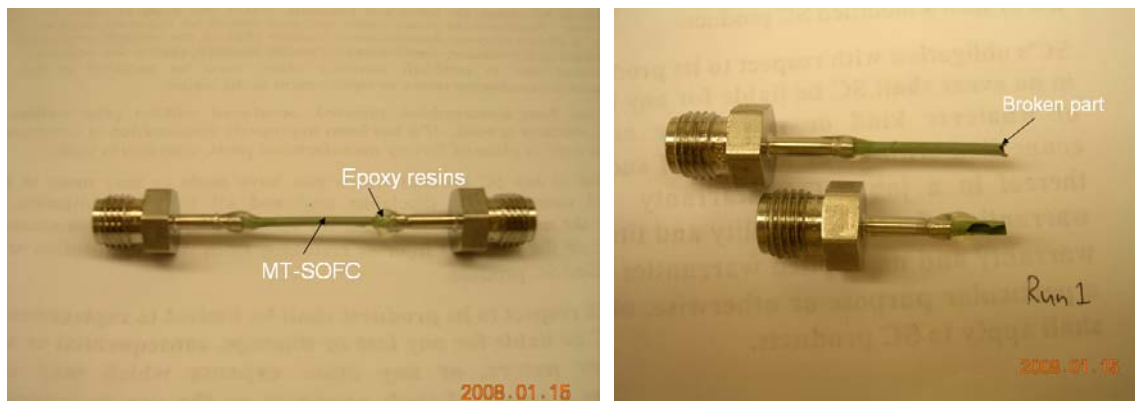


Fig. 9. Loaded micro tubular SOFC into the load cell. The left side indicates the cell before testing (left) and after the right side after testing (right)

Table 1 shows the basic experimental parameters. The effect of sintering temperature, wall thickness, porosity, reducing properties, and electrolyte effect of the cell were tested.

Table 1. Testing parameters for mechanical bursting test

Parameters	Variables
<b>Sintering temperature</b>	1350 °C, 1400 °C
<b>Porosity</b>	40%, 50%
<b>Wall thickness</b>	Average 0.056 mm and Average 0.064 mm
<b>Reduction</b>	Fully reduced, Non reduced
<b>Electrolyte</b>	Existence, Non existence

Fig. 10 shows the burst failure test results of the MT-SOFC. The “standard sample” was sintered at 1400 °C, with a porosity of 40 %, a thin wall thickness (0.056 mm), and under non-reduced conditions. From Fig. 10, two significant effects were observed when each result was compared to the standard SOFC. In other words, the burst strength was found to be significantly dependent on the wall thickness and porosity of the cell. Other effects were not as significant. This indicates that the mechanical properties of MT-SOFC were mainly related to the physical properties of supporting tube.

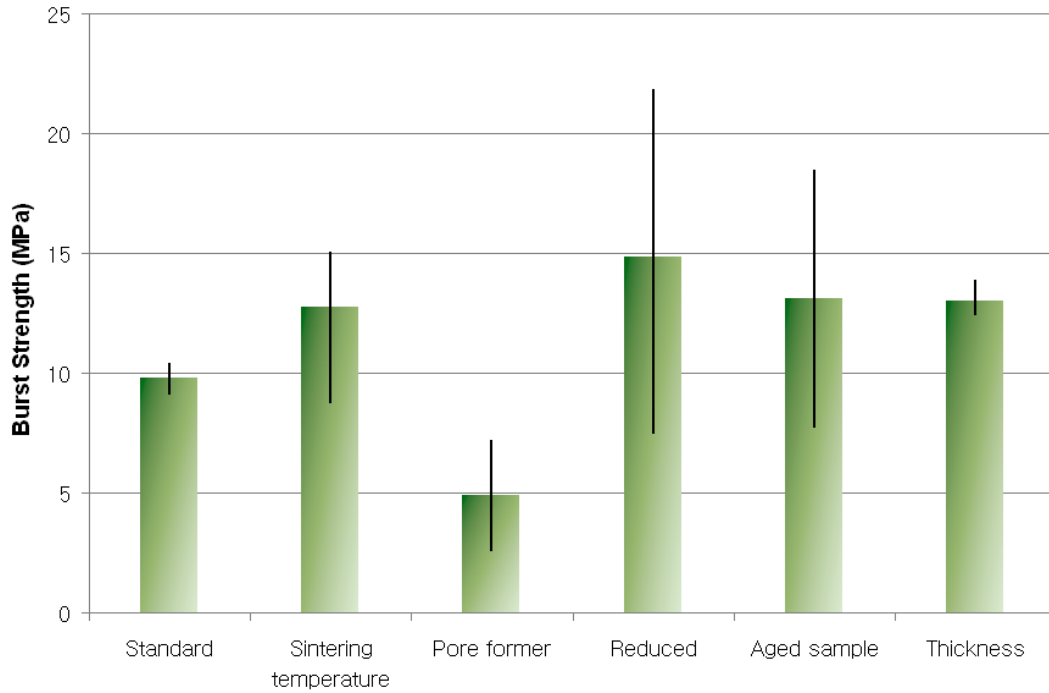


Fig. 10. Effects of materials properties for burst strength

## ELECTROCHEMICAL TESTING

The current collection method is illustrated in Fig. 11. Anode current collector was composed of nickel wire (dia. 0.5 mm). Silver paste was coated using a brush painting technique to reduce the contact resistance of the cell. Cathode current collector was composed of silver wire (dia. 0.5 mm) and was used for winding on the cathode side. The four lines from the cell were connected to the potentiostat (Solartron 1287) under the temperature ranges from 400 to 550 °C. Humidified hydrogen (200 ml/min with 3% H<sub>2</sub>O) was supplied for the anode side. The outside of the cell was exposed to atmospheric conditions. The anode was reduced at 400 °C for 6hrs before measurement of the V-I curves. Impedance evaluation was measured using AC impedance spectroscopy (Solartron 1260) in the frequency range from 100 kHz to 1 Hz with signal amplitude of 10 mV under an open circuit conditions.

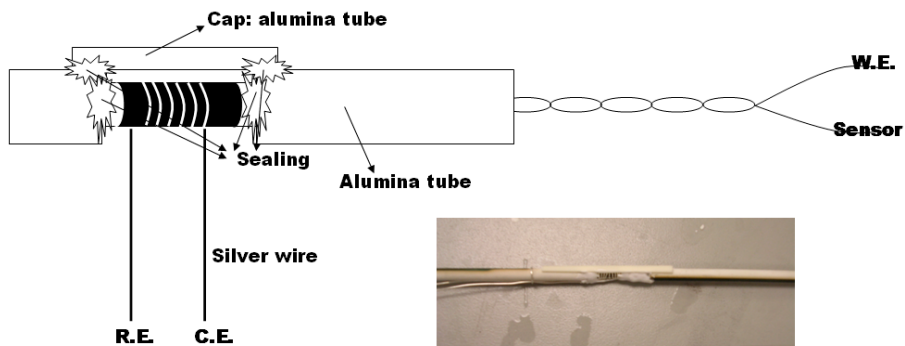


Fig.11. Current-collection method of micro tubular SOFC

The initial behavior of the micro-tubular SOFC is shown in Fig. 12. Fig. 12 shows the OCV with reducing time. It took less than 2 min to reduce the anode and activate the cell at 400 °C, where open circuit voltage reached as high as 1.0 V. This value was very close to that of the theoretical value.

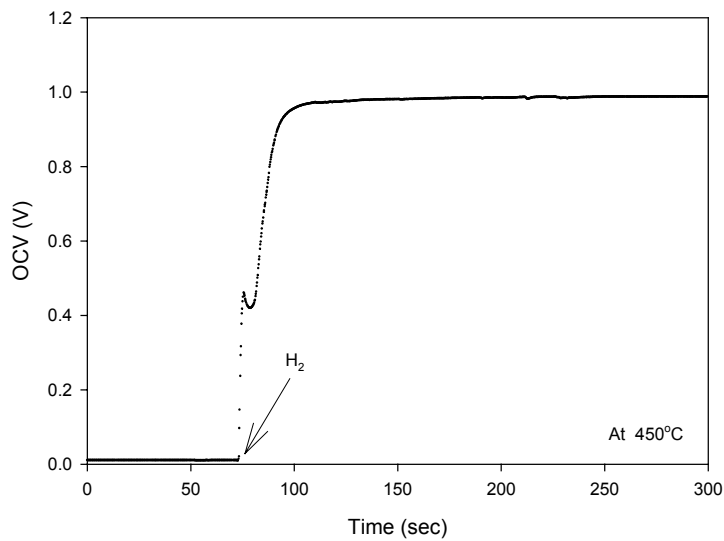


Fig. 12. Initial start-up behavior of the micro tubular cell

The performance of the microtubular cell is observed in Fig. 13. As can be seen, the maximum power density was determined as 0.54, 0.37, 0.13, and 0.09 W at 600, 550, 500, 450 °C respectively. The open circuit voltage dropped from 1.00 to 0.87 V as the temperature was increased. This was explained by an increase in electronic conductivity of the ceria electrolyte at higher temperatures.

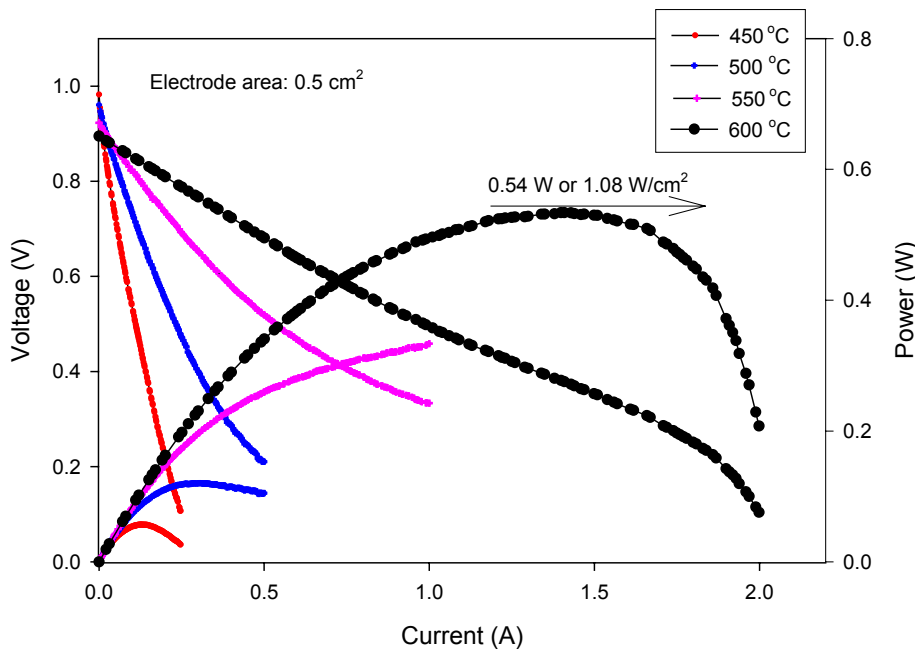


Fig. 13. The performance of microtubular SOFC with different temperature ranges

The impedance spectra is shown in Fig. 14. Ohmic resistance of the cell was determined as  $1.0 \Omega$  and the polarization resistance was determined to be  $2.3 \Omega$  at 500 °C. This value was somewhat larger than the previous study [18]. However, an improvement on the current collection methodology should help this. Fig.15. shows the relationship between  $\ln(T/R)$  and reciprocal temperature determined from Fig. 14. The activation energy was determined from equations 2 and 3. For the electrolyte, the activation energy was 88.1 kJ/mol. This value is somewhat lower than the theoretical value (98.5

kJ/mol), which indicates that the fabricated cell can be improved by reducing the contact resistance between the electrolyte and electrode area [18].

$$\sigma T = A \exp\left(\frac{E_a}{RT}\right), \tag{2}$$

$$\ln(\sigma T) = \ln A + \frac{E_a}{RT} \tag{3}$$

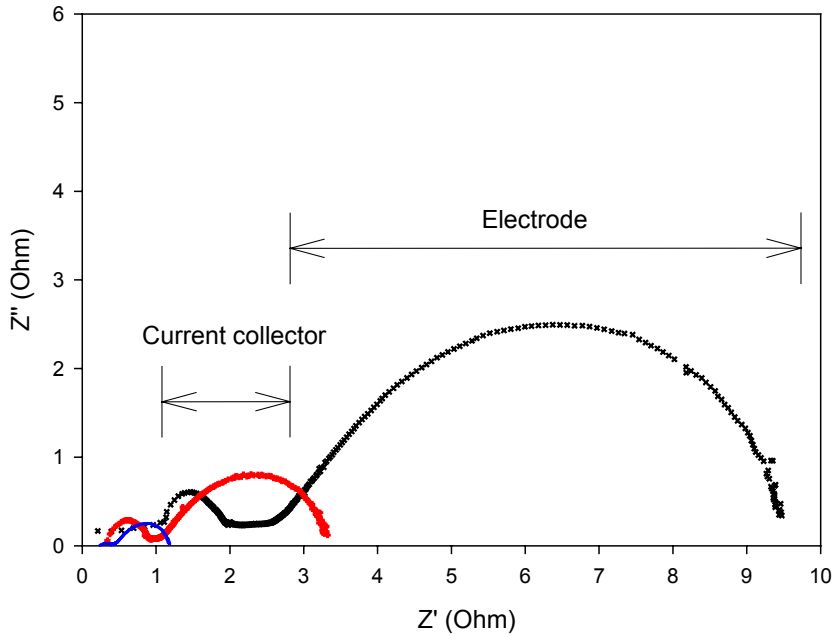


Fig. 14. Impedance spectroscopy of microtubular SOFC

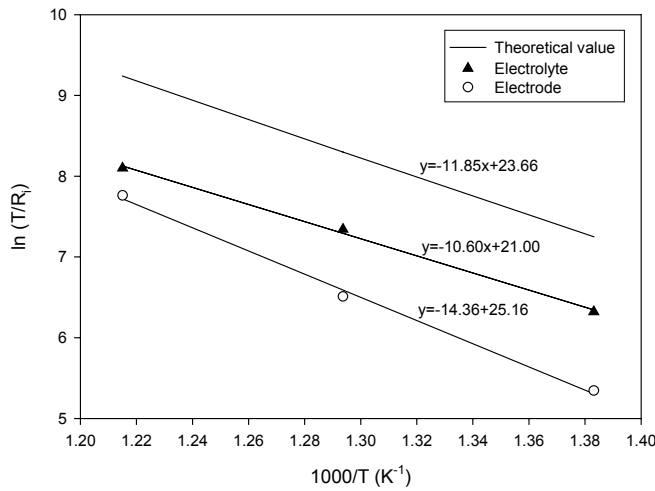


Fig. 15. The relations between  $\ln(T/R)$  and reciprocal of temperature

### Concluding Remarks

Modeling has been performed on the MT-SOFC system including the surrounding heat source. Intriguing results were observed for the system in terms of thermal and electrochemical distribution along the length of the cell. These results should allow for an improvement on the packing of the final stack.

Burst test results were performed to understand better the mechanical properties of the MT-SOFC based on NiO/GDC-GDC-LSCF. The effect of sintering, reduction, porosity, wall thickness, and electrolyte were tested. Among these parameters, anode properties were predominantly influenced by wall thickness and porosity. This indicated that the properties of the supporting materials are the most important parameters to affect its mechanical properties.

Electrochemical testing of MT-SOFCs with 2.0 mm diameter has been successfully investigated in the intermediate temperature region below 600 °C. The results showed that the cell performance was strongly dependent on the contact resistance of the anode side. Also, the reducing time was determined as several minutes due to the small tube diameter. Maximum power density was 1.08 W/cm<sup>2</sup> at 600 °C. The measurement of activation energy of the cell indicated that there are many possibilities to improve the cell performance by reducing the contact resistance between the anode and the electrolyte.

### Acknowledgments

Financial funding was provided by the New Energy and Industrial Technology Development Organization (NEDO) Contract Number AG060145 Advanced Ceramic Reactor Project.

### References

1. Williams M. C., Strakey J. P., Surdoval W. A., Wilson L. C. // *Solid State Ionics*, 2006, Vol. 177, pp. 2039-2044.
2. Masashi M., Yoshiko H., Sammes N.M. // *Solid State Ionics*, 2000, Vol. 135, pp. 743-748.
3. Turner J., Williams M.C., Rajeshwar K. // *Electrochem. Soc. Interface*, 2004, Vol. 13-3, pp. 24-27.
4. Kendall K. and Palin M. // *J. Power Sources*, 1998, Vol. 71, pp. 268-270.
5. Smirnova A., Crosbie G., Ellwood K. // *J. Electrochem. Soc.*, 2001, Vol. 148, pp. 610-614.
6. Pusz J., Mohammadi A., Sammes N. M. // *J. Fuel Cell Sci. and Tech.* 2006, Vol. 3, pp. 482-486.
7. Funahashi Y., Shimamori T., Suzuki T., Fujishiro Y., Awano M. // *J. Power Sources*, 2007, Vol. 163, pp. 731-736.
8. Zhou X., Ma J., Deng F., Meng G., Liu X. // *J. Power Sources*, 2006, Vol. 162, pp. 279-284.
9. Livermore S., Cotton J., Ormerod R. // *J. Power Sources*, 2000, Vol. 86, pp. 411-416.
10. Pal U. B., Gopalan S., Gong W. FY 2004 Annual Report, Office of Fossil Energy Fuel Cell Program, 262 (2004).
11. Sammes N.M., Du Y., Bove R. // *J. Power Sources*, 2005, Vol. 145, pp. 428-434.
12. Fergus J. W. // *J. Power Sources*, 2006, Vol. 162, pp. 30-40.
13. Mogensen M., Primdahl S., Jorgensen M.J., Bagger C. // *J. Electroceram.*, 2000, Vol. 5, pp. 141-145.
14. Mogensen M., Skaarup S. // *Solid State Ionics*, 1996, Vol. 86, pp. 1151-1160.
15. van Berkel F.P.F., van Heuveln F.H., Huijsmans J.P.P. // *Solid State Ionics*, 1994, Vol. 72, pp. 240-247.
16. Yi, J.Y., Choi G. M. // *Solid State Ionics*, 2004, Vol. 175, pp. 145-149.
17. Huijsmans J.P.P., van Berkel F.P.F., Christie G.M. // *J. Power Sources*, 1998, Vol. 71, pp. 107-110.
18. Suzuki T., Yamaguchi T., Fujishiro Y., Awano M. // *J. Power Sources*, 2006, Vol. 160, pp. 73-77.